ADVANCING EARTH AND SPACE SCIENCES

JGR Solid Earth

RESEARCH ARTICLE
10.1029/2024JB029255

# Controls of Grain Breakage on Shear Band Morphology and Porosity Evolution in Fault Gouges

**Qiang Li[1,2], Jianye Chen[3], Chongyuan Zhang[4,5], Liang Yuan[6], Derek Elsworth[7], Quan Gan[1,2], and Fengshou Zhang[8]**

[1]State Key Laboratory of Coal Mine Disaster Dynamics and Control, Chongqing University, Chongqing, China, [2]School of Resources and Safety Engineering, Chongqing University, Chongqing, China, [3]State Key Laboratory of Earthquake Dynamics, Institute of Geology, China Earthquake Administration, Beijing, China, [4]Institute of Geomechanics, Chinese Academy of Geological Sciences, Beijing, China, [5]School of Mechanics and Civil Engineering, China University of Mining and Technology, Beijing, China, [6]State Key Laboratory of Mining Response and Disaster Prevention and Control in Deep Coal Mines, Anhui, China, [7]Department of Energy and Mineral Engineering, EMS Energy Institute and G3 Center, Pennsylvania State University, University Park, PA, USA, [8]Department of Geotechnical Engineering College of Civil Engineering, Tongji University, Shanghai, China

**Abstract** Gouge in fault zones generally undergoes grain breakage during shear slip events, resulting in changes in both shear mode and pore structure. We establish a discrete element model representing shearing of granular fault gouge for increasing normal stresses but constant shear velocity ($v = 6$ μm/s) to investigate the effects of grain breakage on shear band development and the evolution of fault friction and porosity. An increase in normal stress increases frictional strength by ∼20% accompanied by many small slip events triggered by grain breakage. The fragments generated by grain breakage reduce mean grain size and shift the grain size. Dilation and an absence of comminution under low normal stress increase porosity countered by high normal stress developing rapid compaction and grain breakage and decreasing porosity. We propose a concept of porosity evolution linked to volumetric strain. An increase in normal stress results in the principal breakage mechanism evolving from low efficiency abrasion to high efficiency splitting with grain size distribution converging to fractal distributions observed in nature. Heterogeneous grain breakage drives local reduction in porosity, the redistribution of contact stresses and realignment of force-chains, changing the slip pattern and microstructural characteristics through shear band development. At low normal stress, the grain deformation is mainly accommodated by slipping and rolling and the shear bands are dominated by *Y* shears. With the increase in normal stress, grain breakage promotes the development of the more highly inclined *R* shears.

**Plain Language Summary** Fault cores consist of fine-grained gouges formed by the fragmentation of parent rocks on either side of the fault during the repeated shear slip. During shear process, the continuous breakage of fault gouge profoundly impacts the shear mode and porosity of the fault, controlling the frictional strength and stability of the fault. However, understanding the intrinsic relationship linking grain breakage and shear band development with the evolution of porosity and microstructure is still a challenge. In this study, we establish a two-dimensional discrete element model (DEM) accommodating breakable grains during simulated frictional shear to investigate the effects of grain breakage on shear band development and the evolution of fault friction and porosity. Our findings show that an increase in normal stress leads to grain breakage, reduces porosity and increase in macroscopic frictional strength in fault gouge during shear slip. We also analyze the effect of normal stress and shear strain on deformation mechanisms in fault gouge. Heterogeneous grain breakage drives shear deformation localization, changing microstructural characteristics through shear band development. Our research provides new insights into the relationship between grain breakage and shear behavior for various confining stresses.

**Key Points:**

- An increase in normal stress leads to grain breakage, reduces porosity and increases in macroscopic frictional strength in fault gouge during shear slip
- At high normal stress, the principal mechanism gradually transitions from abrasion to splitting
- Grain breakage promotes the development of the more highly inclined *R* shears

**Supporting Information:**

Supporting Information may be found in the online version of this article.

**Correspondence to:**

Q. Gan and C. Zhang,
quan.gan@cqu.edu.cn;
zhchongyuan@126.com

**Citation:**

Li, Q., Chen, J., Zhang, C., Yuan, L., Elsworth, D., Gan, Q., & Zhang, F. (2025). Controls of grain breakage on shear band morphology and porosity evolution in fault gouges. *Journal of Geophysical Research: Solid Earth*, *130*, e2024JB029255. https://doi.org/10.1029/2024JB029255

Received 6 APR 2024
Accepted 15 APR 2025

**Author Contributions:**

**Conceptualization:** Qiang Li, Quan Gan
**Data curation:** Qiang Li, Fengshou Zhang
**Formal analysis:** Jianye Chen
**Funding acquisition:** Quan Gan
**Investigation:** Jianye Chen, Chongyuan Zhang
**Methodology:** Qiang Li, Derek Elsworth, Quan Gan
**Project administration:** Liang Yuan
**Software:** Derek Elsworth
**Supervision:** Liang Yuan, Derek Elsworth, Quan Gan, Fengshou Zhang
**Validation:** Jianye Chen, Chongyuan Zhang, Quan Gan
**Writing – original draft:** Qiang Li
**Writing – review & editing:** Jianye Chen, Chongyuan Zhang, Derek Elsworth, Quan Gan

## 1. Introduction

Fault cores comprise fine-grained gouges that evolves from the abrasion and fragmentation of the parent rock mass during large scale fault slip and control the frictional strength and stability of the fault (Billi et al., 2003; Dor et al., 2006; Muto et al., 2015). In fault zones, most of the shear deformation is localized within fault core and indeed results from the long-term accumulation of grain breakage (Boulton et al., 2017; Scuderi et al., 2017). This continuous evolution of grain size distribution and morphology during the shearing process profoundly alters the frictional and mechanical properties and porosity of the fault (Storti et al., 2003; Zhang et al., 2020).

Microstructures evolve continuously but episodically with slip and are manifest as shear bands and are indicative of strain paths (Balsamo & Storti, 2010; Del Sole & Antonellini, 2019; Pizzati et al., 2020). Such micro-to macro-scale features resulting from grain breakage and microstructural evolution are often correlated with the deformation and strength of the fault and can be used to further understand slip behavior (Han et al., 2010; Kuo et al., 2014; Smith et al., 2011).

Observations of frictional sliding in gouge, particularly at high confining stresses, display significant grain breakage reflected in a widening grain size distribution and a change in grain angularity (Anthony & Marone, 2005; Hunfeld et al., 2017; Mair et al., 2002). These changes affect the frictional properties and microstructure of the fault gouge (Anthony & Marone, 2005; Hunfeld et al., 2017) - an increase in grain angularity increases both frictional strength and stability at high confining stresses (Anthony & Marone, 2005). The increase in the number of fine grains, due to breakage, facilitates a more pronounced strain localization (Marone & Scholz, 1989; Shigematsu et al., 2004). Microstructural studies confirm that the formation of shear bands is often accompanied by an increase in porosity. However, numerous experiments have demonstrated that the development of shear bands may be accompanied by dilation at low stresses, compaction at high stresses, or may exhibit more complex volumetric evolution, depending on the initial density of the granular material, its particulate strength and the confining pressure applied to the samples (Alikarami et al., 2015; De Paola et al., 2015; Scuderi et al., 2017). Many experimental observations demonstrate a correlation between grain breakage and fault strength and shear band evolution, but are generally limited to post-experiment visualization of terminal grain-scale deformation and evolved microstructures. Visual shear experiments are mainly limited to low effective stresses and thus without significant grain breakage, and concurrent imaging with shear is hindered by issues in the spatial and dynamic resolution of the microstructures (Fukuoka, 1991; Fukuoka et al., 2007; Li et al., 2024). Conversely, discrete element methods (DEM) offer the facility to follow evolution of strength and structure through the shearing process and to link these to rheologic signals in experiments that thus infer the normally unseen evolution of microstructure. Thus, DEM methods have been widely applied in the study of granular material breakage and shear localization (Gu et al., 2014; Liu et al., 2018; Long et al., 2018; van den Ende & Niemeijer, 2018; Wang & Yan, 2012).

Two-dimensional DEM models of shear slip indicate that the incorporation of angular grains better matches laboratory observations of frictional rheology, and that the production of fine grains and resulting inter-grain friction both promote transient strain localization (Morgan & Boettcher, 1999a). Three-dimensional DEM models containing breakable grains have reproduced the evolution of grain breakage during gouge shear with high fidelity (Abe & Mair, 2005). Different degrees of grain breakage also affect the deformation mechanisms that evolve in faults. Fragments may be angular, inhibiting intergranular sliding and rolling, or they may also eventually evolve into smaller, rounded grains, accommodating greater deformation (Guo & Morgan, 2006). Focusing on grain breakage, studies considering the relationship between grain size distribution, fragment shape and shear strain localization, demonstrate a close correlation between grain size reduction and strain localization. These elaborate on the link between the two breakage mechanisms of grain splitting and abrasion (Abe & Mair, 2009; Mair & Abe, 2008, 2011). However, more detailed understanding of the linkage between grain breakage and strain localization, especially on the effect on microstructure (e.g., $Y$ shears vs. $R$ shears) is absent. Observed changes in local porosity have been used to study shear strain localization and impacts of grain modulus, intergranular friction and fault gouge thickness on the evolution of Riedel shear bands in over-consolidated faults (Casas et al., 2023). In addition, velocity-stepped three-dimensional DEM simulations have explored the effects of mineral distribution and content on the evolution of shear localization and permeability (Wang et al., 2019). They recognize the correlation between shear band formation and the evolution of porosity, although grain breakage during slip—the principal focus of our interest here—has not been considered. Therefore, a robust intrinsic relationship linking grain breakage and shear band development with the evolution of porosity and microstructure remains elusive.

Shear bands in poorly lithified sandstones and fault fracture zones have been observed in many geological locations (Schultz et al., 2010; Torabi et al., 2007), with microstructural evidence of porosity reduction and grain breakage (Shahin & Hurley, 2022; Wong & Baud, 2012). Based on laboratory experiments with glass beads (Mair et al., 2002), we establish a two-dimensional discrete element model (DEM) accommodating breakable grains during simulated frictional shear. First, we analyze the effect of normal stress on the evolution of frictional strength and porosity. Then, we explore the effect of grain breakage on the evolution of shear bands and microstructures through strain localization. This work quantifies the important controls of normal stress and shear

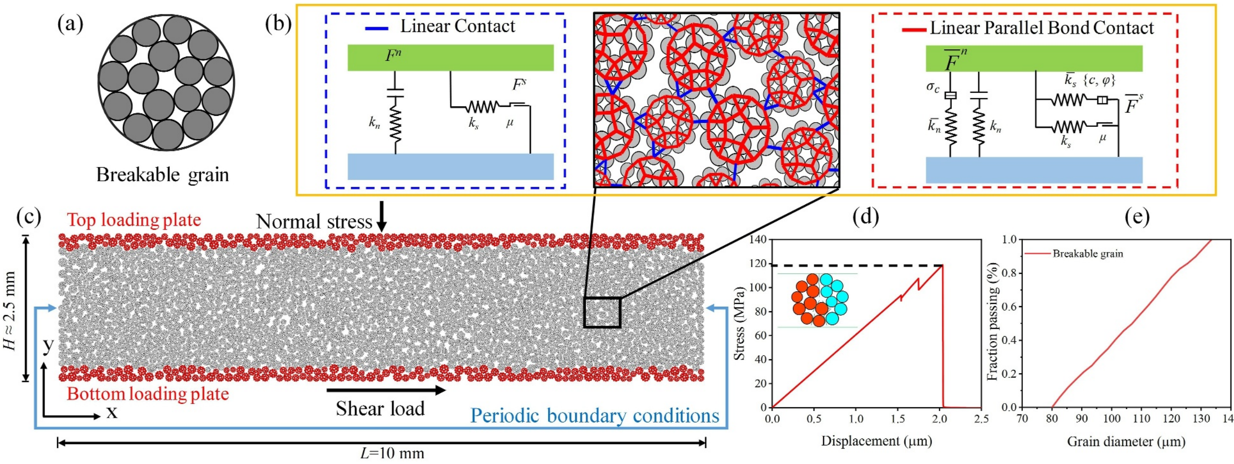

**Figure 1.** Modeling of shear-slip in a gouge filled fault: (a) Breakable grain. (b) Intra-grain and inter-grain contact model. (c) Fault gouge shear model. (d) Single grain compression damage simulation. (e) Breakable grain distribution.

strain on deformation mechanisms in fault gouge, providing new insights into the relationship between grain breakage and shear behavior for various confining stresses.

## 2. Methods

We generate a grain template by populating a circular container with particles in the DEM code PFC (Itasca Consulting Group Inc, 2019). The circular container has the final size of the cluster. However, to achieve rapid equilibration, the sizes of some particles are scaled to eliminate the initial overlap among particles (Wang & Yan, 2013). Then, Linear Parallel Bonds are installed at all the particle-particle contacts to form an ensemble breakage grain (Figure 1b). This cluster method accurately captures the characteristics of grain breakage, and has been widely used in DEM modeling of geotechnical granular media (Bolton et al., 2008; Cheng et al., 2003; Wang & Yan, 2013; Zhang et al., 2023). The bead-pack particle-assembly (gouge) is mainly quartz with a critical grain compressive strength decreasing with grain size from 110 to 147 MPa (Nakata et al., 2001). We perform simulations of one-dimensional compression and calibrations on single strong and brittle grains (Figure 1d) to replicate these grain strengths. Meanwhile, simulations of direct shear with grain aggregates are carried out to verify the accuracy of the contact parameters. The contact parameters are as detailed in Table 1.

The Linear Parallel Bond Model (LPBM) can bond a cluster of smaller particles into a cluster through adhesive bonds with a defined footprint, as shown in Figure 1b. The LPBM can survive threshold forces in shear and tension and bending moments before failing and allowing for grain breakage (Itasca Consulting Group Inc, 2019; Potyondy & Cundall, 2004). The contact is ruptured by tensile failure, once the maximum tensile stress exceeds the tensile strength, as follows:

$$\overline{\sigma} = \begin{cases} \dfrac{\overline{F}^n}{\overline{A}} + \overline{\beta}\dfrac{\|\overline{M}_b\|\overline{R}}{\overline{I}} & \overline{\sigma} \le \sigma_c \\ 0 & \overline{\sigma} > \sigma_c \end{cases} \quad (1)$$

where $\overline{F}^n$、 $\overline{A}$、 $\overline{\beta}$、 $\overline{M}_b$、 $\overline{R}$ and $\overline{I}$ are contact normal force, contact area, bending moment coefficient, contact bending moment, particle radius, moment of inertia and contact tensile strength, respectively.

If the shear stress exceeds the maximum shear strength $\tau_{\max} = c - \sigma \tan \varphi$, the contact will rupture in shear. After the bonded contact breaks, it degrades to a linear contact and the contact will only respond in Coulomb slip in the tangential direction (Itasca Consulting Group Inc, 2019; Zhang et al., 2022), as Equation 2:

**Table 1**
*Parameters Used in the DEM Simulations (Lin et al., 2020)*

| Mesoscopic parameter | Value | Unit |
|---|---|---|
| Effective modulus | 15 | GPa |
| Normal-to-shear stiffness ratio | 1.2 | 1 |
| Particle friction coefficient (Intergranular) | 0.1 | 1 |
| Tensile strength | 320 | MPa |
| Cohesive strength | 160 | MPa |
| Particle friction coefficient (Intragranular) | 0.15 | 1 |
| Friction angle | 30 | ° |

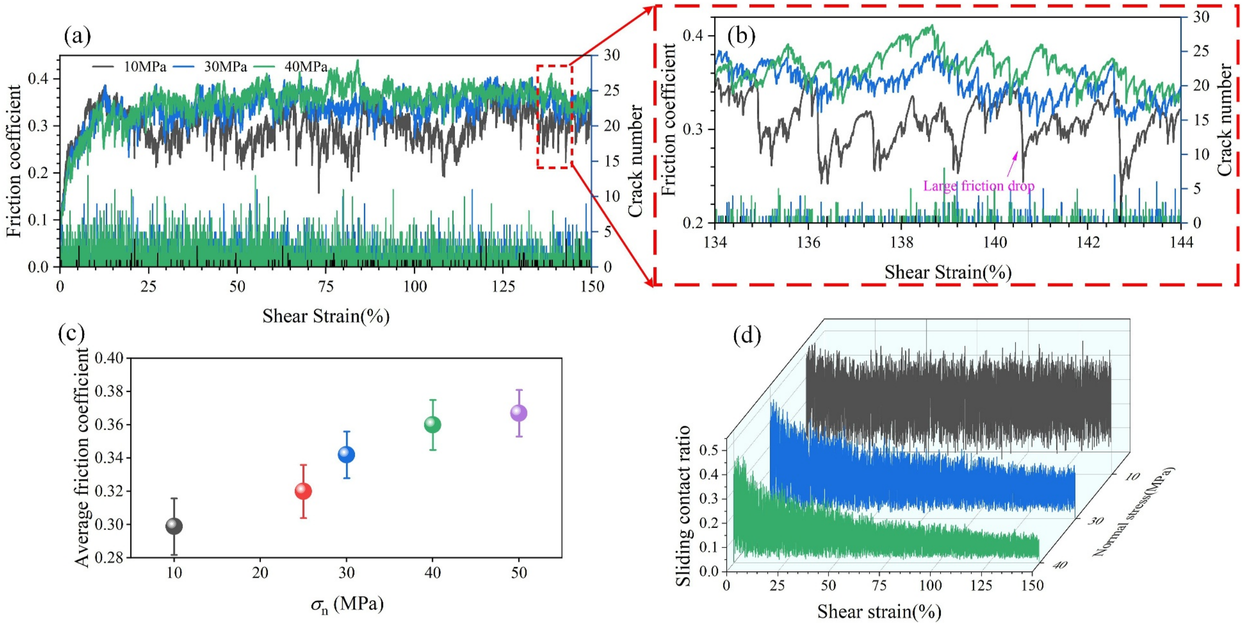

**Figure 2.** Comparison of macroscopic friction coefficients and number of cracks per unit time between samples at different normal stresses: (a) Macroscopic friction. (b) Marked inset in (a). (c) Average friction coefficient. (d) Evolution of sliding contact ratio.

$$\overline{\tau} = \begin{cases} \dfrac{\overline{F}^s}{\overline{A}} + \begin{cases} 0 \quad (2D) \\ \overline{\beta}\dfrac{\lVert \overline{M}_t \rVert \overline{R}}{\overline{J}} \; (3D) \end{cases} & \overline{\tau} \le \tau_{\max} \\ \mu\overline{\sigma} & \overline{\tau} > \tau_{\max} \end{cases} \tag{2}$$

where $\overline{F}^s$、 $\overline{M}_t$、 $\overline{J}$、 $\mu$、 $c$ and $\varphi$ are the contact tangential force, contact torque, contact friction coefficient, cohesive force, and contact internal friction angle, respectively.

The gouge shear sample is 10 mm long and ~2.5 mm thick (Figure 1c). The equivalent grain diameter of granular layer ranges from 80 to 134 μm with a uniform distribution (Figure 1e). Rigid clumps of grains the same size as the fault gouge are used to represent the loading platens sandwiching the top and bottom of the sample. The friction coefficient between the plates and the grains is set at 1.0 to enforce a no-slip boundary and to ensure that the deformation is distributed throughout the full thickness of the fault (Dorostkar & Carmeliet, 2019). Periodic boundary conditions are set to the left and right sides of the sample to represent shear displacement in an infinite length fault and to eliminate variations in the results due to changes in the shear area, as shown in Figure 1c. Intergrain contacts are represented by a Linear Contact Model to represent unbonded grains. The initial intergranular friction coefficient is set as a low value of 0.1. In reality, an increase in macroscopic friction from 0.45 to 0.6 arises from broken particles with higher angularity and roughness (Mair et al., 2002). We increase the intergranular friction from 0.1 for the original grains to 0.9 for the broken grains to follow the dominant role of micro- to macro-scale roughness or "geometric friction" of the broken particles after breakage. This approach has been successfully validated for DEM simulations (Mollon et al., 2020; Wang et al., 2021). Additionally, previous studies have demonstrated that the introduction of rolling friction rapidly stabilizes stick-slip dynamics, leading to a gradual decrease in the macroscopic friction (Dorostkar & Carmeliet, 2019). To focus on the effect of intergranular friction on broken grains, this study excludes the influence of rolling friction by setting it to zero.

The stiffness ratio of spherical particles is typically within the range ~1.0–1.5 (Goldenberg & Goldhirsch, 2005; Nie et al., 2023), and we select a value of 1.2. Grain breakage is observed to be minimal at normal stresses below 10 MPa (shown in Figure 2a), consistent with the response of the DEM breakage grains (Anthony & Marone, 2005).

Consistent with laboratory experiments, the position of the top plate is stress-feedback-controlled during the simulation to apply a constant normal stress (10–50 MPa). Once at the prescribed normal stress, the top plate is locked from travel in the $x$-direction and the bottom plate sheared in the $x$-direction at constant velocity ($v = 6$ μm/s) until a shear strain of ∼1.5 is reached. Since we are interested only in quasi-static response particle density is inflated to 2,650 × $10^8$ $m^3$/kg for density scaling used to increase the simulation timestep ($\Delta t \propto \sqrt{m/k}$) and to thereby overcome limitations of computational effort (Ferdowsi et al., 2014; O'Sullivan & Bray, 2004; Thornton, 2000; Wang et al., 2019). The inertia number $I$ is an important index characterizing the dynamic response of granular materials and is given by (Koval et al., 2009; MiDi, 2004; Papachristos et al., 2023)

$$I = \dot{\gamma} d \sqrt{\frac{\rho}{P}} \tag{3}$$

where $\dot{\gamma}$ is the shear rate, $d$ is the average particle size, $P$ is the pressure (normal stress here) and $\rho$ is the particle density. We retain the inertia number $I < 10^{-5}$ throughout the simulations, significantly lower than $10^{-3}$, maintaining the simulation in the quasi-static region where the density scaling effect can be neglected. The effect of gravity is neglected in the subsequent analysis as applied stresses are high in comparison to stress gradients induced by self-weight.

## 3. Results

### 3.1. Mechanical Behavior

Figure 2 illustrates the evolution of the macroscopic friction coefficient (defined as the ratio of the shear stress to normal stress) and crack numbers per unit time for different normal stresses ($\sigma_n$ = 10, 30, and 40 MPa). The macroscopic friction coefficients all increase nonlinearly and evolve into stick-slips after reaching a critical state. At $\sigma_n$ = 10 MPa, only a few cracks develop and with little grain breakage (Figure 2a). As the normal stress increases, numerous cracks develop and grain breakage initiates and gradually increases. The macroscopic friction coefficient asymptotes to a stable level when the strain reaches ∼60%. We select the friction coefficient after 60% shear strain for comparison against the average macroscopic friction coefficient (Figure 2c). The average macroscopic friction increases nonlinearly with an increase in normal stress, suggesting a strengthening effect driven by continuous grain breakage. This is consistent with experimental observations of Mair et al. (2002) and the numerical results of Wang et al. (2021). As normal stress increases, the greater number of broken grains exhibit higher surface roughness and sharper edges. In our simulation, this is represented by higher inter-grain friction coefficients and the evolving geometric angularity of the fragments. Fault gouge evolves to higher frictional strengths due to the existence of angular grains (Anthony & Marone, 2005), consistent with our simulations (Figure 2c). It should be noted that the macroscopic friction in our model is lower than the values found in these experiments (Anthony & Marone, 2005; Mair et al., 2002), likely because the evolving geometry of the grains is more important in determining macroscopic friction than the inter-granular friction and the 2D model does not fully reproduce the grain geometry (Frye & Marone, 2002; Mora & Place, 1998).

The fine scale resolution of friction with shear strain (Figure 2b) shows the greatest amplitude and several large macroscopic friction drops (>0.05) for $\sigma_n$ = 10 MPa. Since there is negligible grain breakage, such large slip events must originate from the structural rearrangement between grains. Grain breakage increases with normal stress but the amplitude of the fluctuation in friction coefficient significantly decreases—as small but frequent small slip events occur. The numerous unstable small slip events are accompanied by a gradual decrease in large slip events as normal stress increases. This change of friction stability caused by normal stress enhancement is basically consistent with the experimental tests of Mair et al. (2002).

The characteristics of slip events can be studied through the evolution of contact force chains (Aharonov & Sparks, 2004). The calculation of contact force orientation anisotropy is shown in Equation 4. Strong contact forces identified by force chains are highly anisotropic ($a_n = 0.43$) in the stick phase, with a dominant orientation of ∼50° (Figure 3d). During slip events, some of these strong contact force chains are completely destroyed by the shear deformation (Figures 3b and 3c), yet high anisotropy is retained ($a_n$ = 0.35). However, after the accumulation of shear stress, the weak contact forces remain oriented perpendicular to the strong force chains, at ∼140°(Figure 3e), providing lateral support to the strong force chains. After stress release, the anisotropy of the weak contact forces decreases significantly and their orientation becomes more random. The rearrangement of

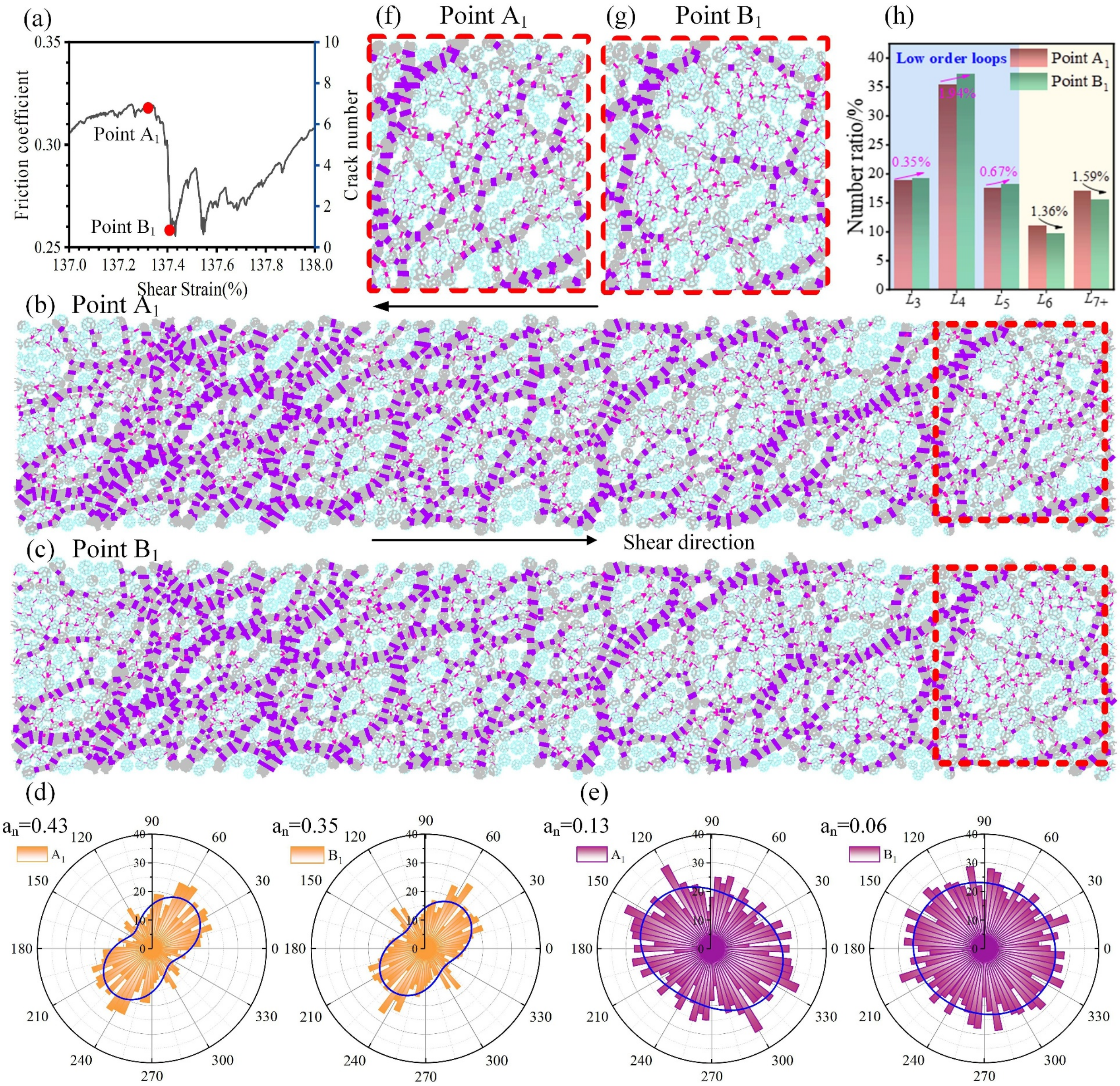

**Figure 3.** (a) Typical time series of macroscopic friction at at $\sigma_n = 10$ MPa. Spatial distribution of contact force chains (purple lines represent the intergranular contacts carrying forces larger (strong) than the mean, pink lines are intergranular contacts carrying forces smaller (weak) than the mean, and gray lines are the intragranular contacts, with thickness increasing with force): (b) Point $A_1$, (c) Point $B_1$. Rose diagrams of intergranular contact orientations: (d) contacts with large contact forces (defined here to be those with a force at least 1.25 times the average contact force), (e) contacts with small contact forces (defined here to be those with a force at least 0.75 times the average contact force). (f) Marked in (b). (g) Marked in (c). (h) Number ratio of different Loops.

grains leads to the collapse of some strong force chains, reducing the support from weak chains and triggering the occurrence of stress drops.

$$E(\phi) = E_0\{1 + a_n \cos 2(\phi - \phi_n)\} \tag{4}$$

where $E_0$ denotes the distribution probability density function at an isotropic state, $a_n$ is a second-rank tensor describing the deviations from the isotropic distribution, $\phi$ refers to a direction angle of interest and $\phi_n$ indicates the principal direction of anisotropy.

Grain breakage leads to a more complex contact force network (Figure S2 in Supporting Information S1; $\sigma_n = 40$ MPa). Slip events are accompanied by grain breakage, resulting in a slight decrease in the anisotropy of

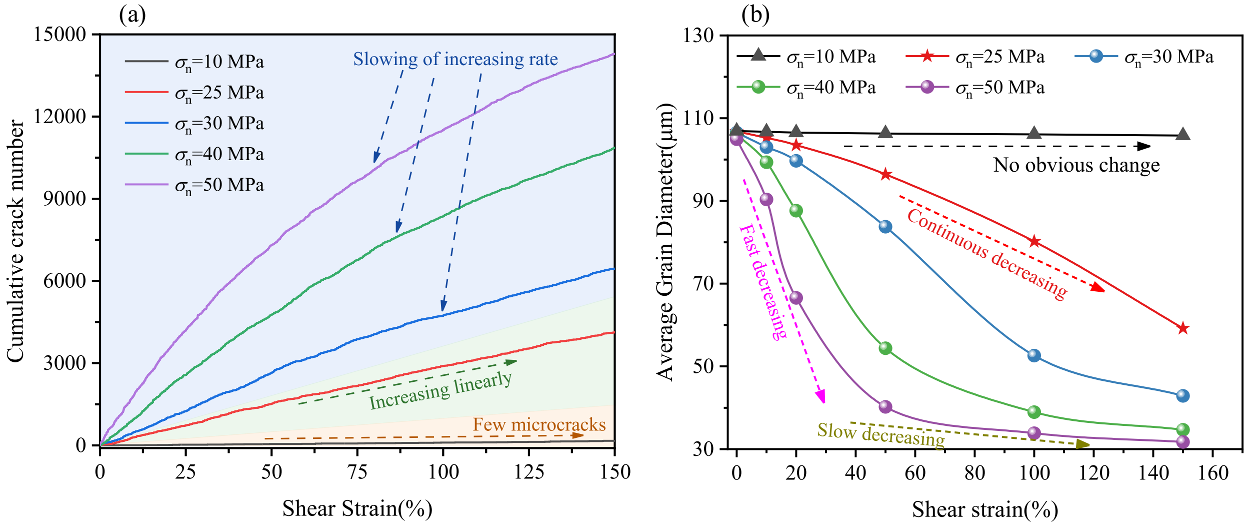

**Figure 4.** Evolution with shear strain of (a) Cumulative crack numbers. (b) Average grain sizes.

both strong and weak contact forces. Compared to $\sigma_n = 10$ MPa, the strong force chains endure. The ongoing breakage of grains enhances the stability of the contact force chains. Localized grain breakage prevents the strong force chains from becoming entirely unstable, thereby reducing the magnitude of stress drops and enhancing the frictional stability.

To qualitatively analyze the local mechanical behaviors of the mesoscopic structures, the Loop structure is classified as $L_i$ ($i = 3, 4, 5, 6, 7+$), that is, a "Loop" comprises a closed polygon forming by $i$ contact grains. The ratio of the number of low order loops ($i = 3$, 4 and 5) that dominate in the contact topological structure is greater than that of high order loops ($i \geq 6$), which is consistent with previous studies (Zhu et al., 2016). During the shearing, the strong force chains formed by high order Loops support relatively large loads, while the evolution of low order Loops may be related to weak force chains (Liu et al., 2020; Zhu et al., 2016). At $\sigma_n = 10$ MPa, the stress accumulation process leads to a higher ratio of high order Loops (Figure 3h). The transformation from high order Loops to low order Loops induces the instability of the system. Compared to $\sigma_n = 10$ MPa, there is a higher ratio of low order Loops (Figure S2h in Supporting Information S1, $\sigma_n = 40$ MPa), presenting a relatively uniform stress distribution (Liu et al., 2020). The local instability of force chains and the lower failure ratio of high order Loops reduce the magnitude of stress drop.

The sliding contact ratio (SCR) is defined as the ratio of the number of contacts in which sliding occurs to the total number of contacts. The grain SCR remains at ~0.35 and shows a relatively high sliding ratio at $\sigma_n = 10$ MPa. The ratio of grain sliding decreases with increased stress then decreases nonlinearly with an increase of shear strain. The broken grains with high friction coefficient and high angularity reduce the SCR, leading to an increase in interlocking between grains finally resulting in an increase in macroscopic friction coefficient. After reaching a shear strain of 100%, the SCR gradually stabilizes, converging to ~0.12 at $\sigma_n = 30$ MPa and ~0.06 at $\sigma_n = 40$ MPa. At higher shear strains, the degree of grain breakage gradually reaches the maximum, leading to a gradual stabilization of the SCR.

The evolution of average grain size is closely related to applied normal stress and evolved shear strain (Figure 4). An increase in normal stress results in a large number of microcracks and grain breakage and the average grain size decreases significantly. In general, there is a little grain breakage with $\sigma_n = 10$ MPa, so the average grain size does not change significantly with increasing shear strain. At $\sigma_n = 25$ MPa, the average grain size decreases uniformly with an increase in shear strain. The higher normal stress results in a more rapid decrease in grain size and smaller residual grain size. Compared with $\sigma_n = 25$ MPa (Figure 5a), higher normal stress results in relatively higher breakage of large-sized grains and the formation of small and medium-sized grains, increasing the total abundance of grains (Figures 5b–5d). After 100% shear strain, grain breakage is very slow, tending toward a stable steady-state gradation (Figure 5d).

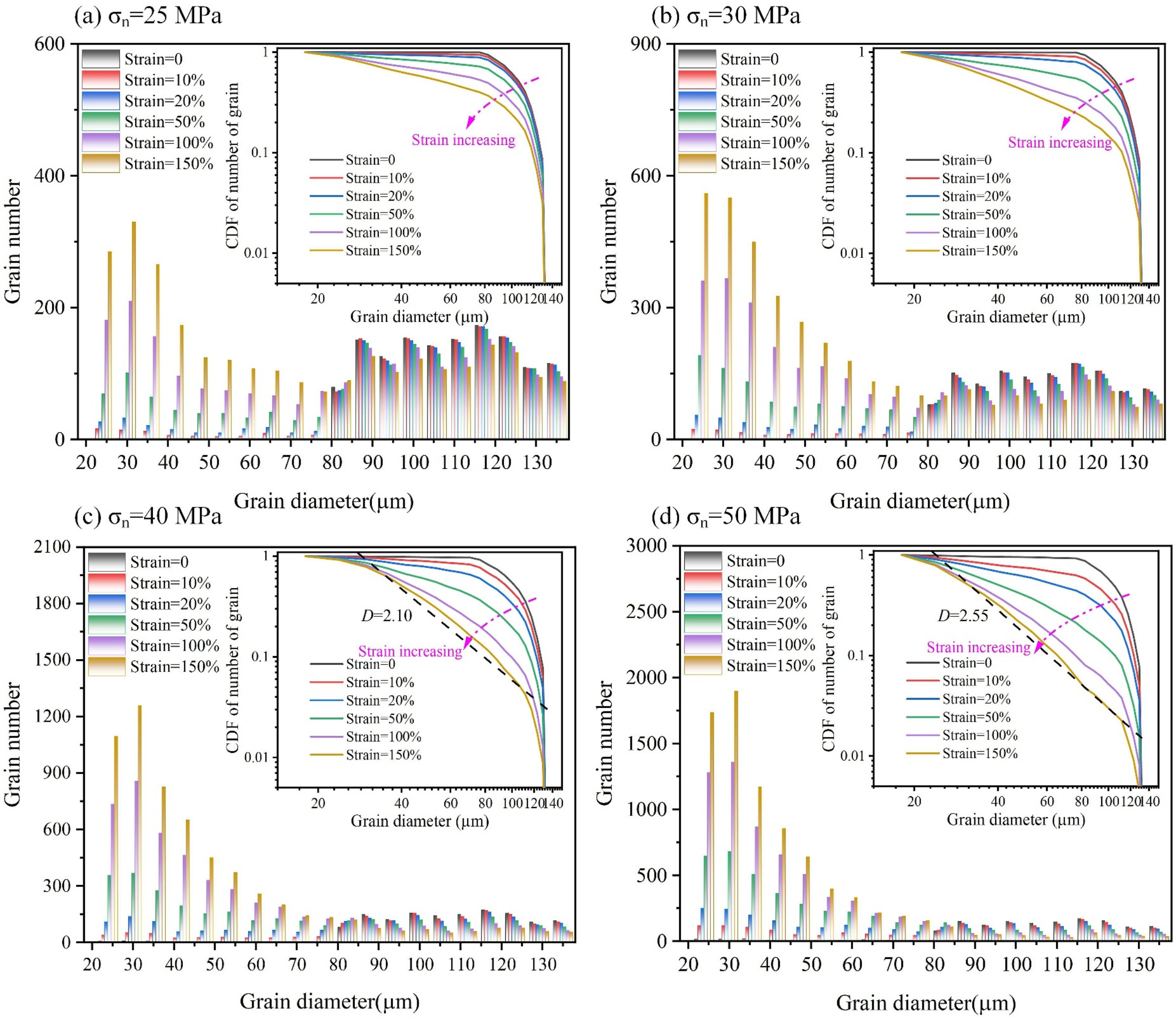

**Figure 5.** Evolution of grain gradations under different normal stresses.

To better describe the evolution of the grain size resulting from mechanical deformation, we use the fractal dimension $D$ to represent the response of the grain size distribution (Turcotte, 1983):

$$N_{\mathrm{cum}} \propto R^{-D} \tag{5}$$

where $N_{\mathrm{cum}}$ represents the cumulative total number of grains with grain sizes larger than $R$, where $R$ is the target grain size. The grain size-number in numerous natural fault gouges follows a fractal distribution with the fractal dimension $D$ of the fault gouge typically ranging from 2.5 to 2.7 (Billi et al., 2003; Marone & Scholz, 1989). At $\sigma_n = 50$ MPa (Figure 5d), the grain aggregate reaches its stable state with a final fractal dimension $D = 2.55$ (more than 90% of the grains show a fractal distribution). As shown in Figures 5a–5c, with the increase in normal stress, the potentially stable state is reached more rapidly. Figure 5 shows that the evolution of the grain size is similar to that of fault gouge in experiments (Marone & Scholz, 1989; Ran et al., 2022).

### 3.2. Evolution of Thickness and Porosity

Dilation or compaction during fault reactivation depends on the mechanical properties of the granular material and stress conditions. Changes in gouge thickness result from both grain rearrangement and breakage, which can alter the porosity of the fault gouge. We follow mean dilation or compaction by monitoring changes in gouge layer

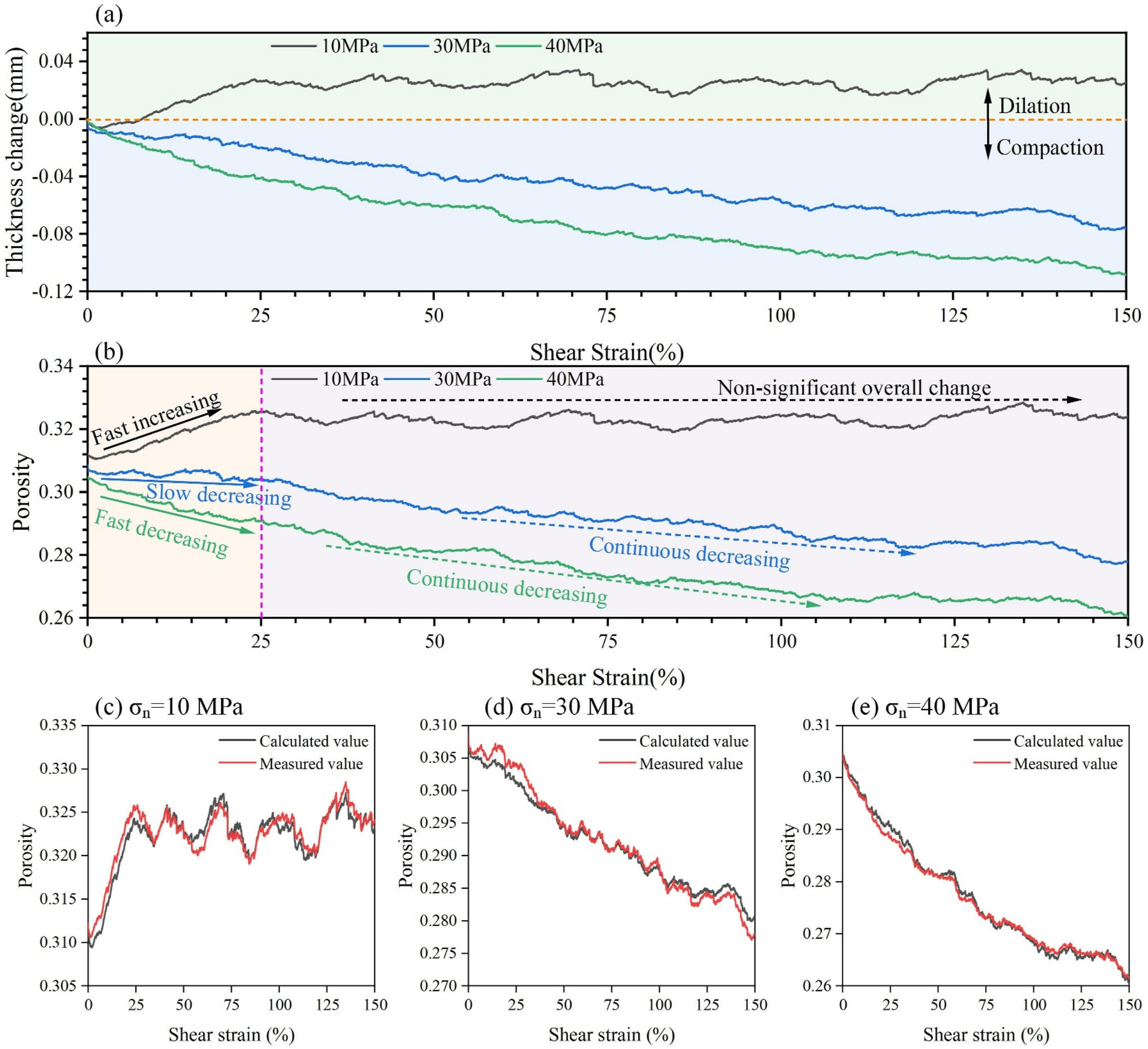

**Figure 6.** Evolutions with shear strain of (a) Change in thickness. (b) Porosity. (c)–(e) Porosity compared between measured and calculated.

thickness, with porosity evolution determined from real-time monitoring in distributed sampling circles during shear slip.

Figures 6a and 6b illustrate the evolution of thickness and porosity of the sample under different normal stresses. At higher normal stresses the thinner and lower the initial porosity of the layer—due to compaction. At $\sigma_n = 10$ MPa, the sample compacts rapidly (∼2% shear strain) before then dilating and increasing porosity. The sample oscillates in dilation-compaction about a mean and the porosity responds similarly. This pattern of slip at low stress describes the process of grain frictional interlocking. An increase in the friction coefficient and subsequent dilation increases porosity, before failure due to sudden sliding between grains with a geometric loss of interlock. Friction then rapidly decreases, followed by gouge compaction—consistent with experimental observations (Lyu et al., 2019). As normal stress increases, the gouge compacts monotonically with the evolution of porosity at $\sigma_n = 30$ MPa, initially decreasing slowly before a fast and continuous decrease. At $\sigma_n = 40$ MPa, there is a rapid decrease in porosity, resulting from significant grain breakage. The larger the normal stress, the more significant the grain breakage, with the derived small fragments infilling the pores—precipitating this response. In this process, volume compression due to grain breakage dominates, which offsets the effect of the volume dilation due to grain rearrangement (Wang & Yan, 2013).

Porosity $\phi$ may be estimated as a function of volumetric strain $\varepsilon_v$ (Chin et al., 2000; Rinaldi et al., 2014):

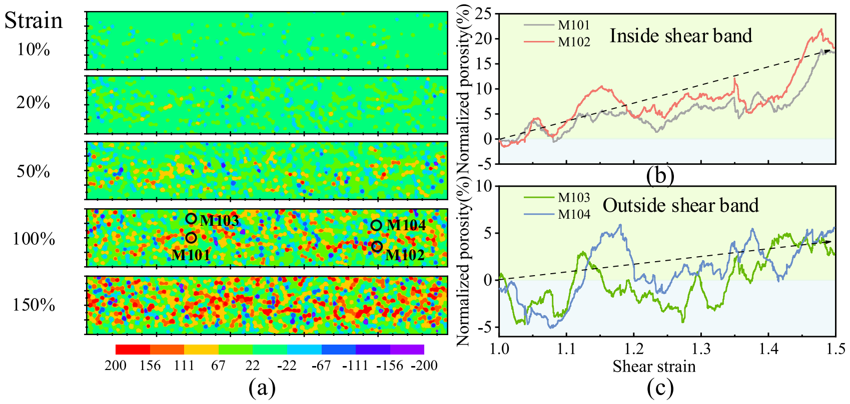

**Figure 7.** Maps of: (a) Cumulative grain rotation (Unit: °) with shear strain. (b) and (c) Evolution of normalized porosity inside and outside the shear band at shear strains of 1.0–1.5 at $\sigma_n = 10$ MPa.

$$\phi = 1 - (1 - \phi_0)\, e^{-\varepsilon_v} \tag{6}$$

The porosity evolution recovered from the volumetric strain matches the porosity evolution measured using the circular measurement windows, with an error of less than 1% (see in Figures 6c–6e).

### 3.3. Shear Band Evolution

The shear band can be identified by some characteristic parameters of the gouge, including porosity, cumulative particle rotation and relative displacement (Zhou et al., 2017). Shear bands can often be distinguished by particle rotations, with cumulative particle rotation often used as an identifier for shear band localization in granular materials (Gu et al., 2014). Shear bands gradually mature as the shear strain increases from 1.0 to 1.5 (Figures 7–10). We set several circular measurement windows both in and outside the shear band to obtain the normalized void ratio (with positive values indicating an increase in porosity). At $\sigma_n = 10$ MPa, grain breakage rarely occurs and the shear strain is accommodated mainly by inter-grain slip and rolling—as a result the fault dilates, the average porosity increases and the grain size does not change significantly. The grain rotation is mainly distributed in the center of the fault gouge at 10% shear strain (Figure 7a). Grain rotation gradually increases with increased shear strain, and multiple thin shear structures develop. After 100% shear strain, multiple small shear structures gradually connect to form a sub-horizontal shear band. Dilation occurs both inside and outside the shear band due to grain rearrangement (Figures 7b and 7c). The shear band localizes shear strain, resulting in a more pronounced dilation effect due to macroscopic roughness (Figure 7b). In addition, with increasing of shear strain, continuous grain rearrangement drives an increase in porosity and a more heterogeneous porosity distribution is reflected in an increased standard deviation (Figure 8a).

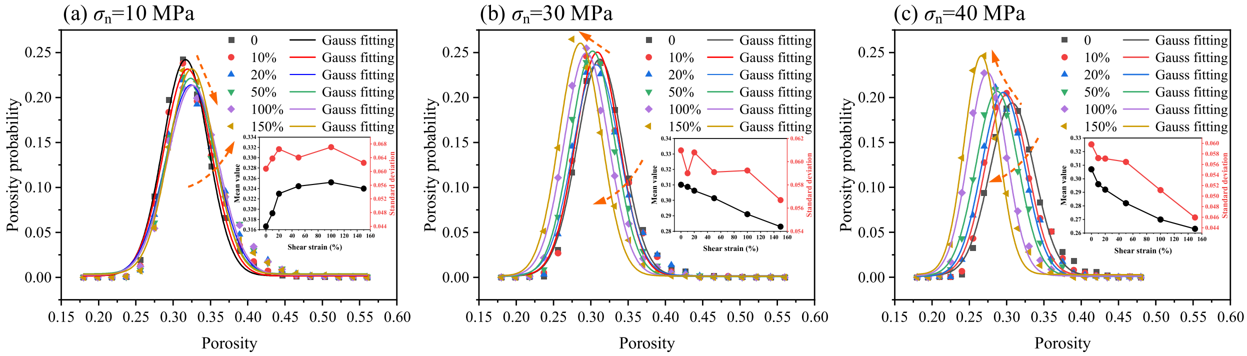

**Figure 8.** Distribution of porosity of fault gouge under different shear strains (The probability distribution of porosity follows a Gaussian distribution function. Mean Value represents the average porosity and Standard deviation represents the dispersion of the porosity distribution.): (a) $\sigma_n = 10$ MPa. (b) $\sigma_n = 30$ MPa. (c) $\sigma_n = 40$ MPa.

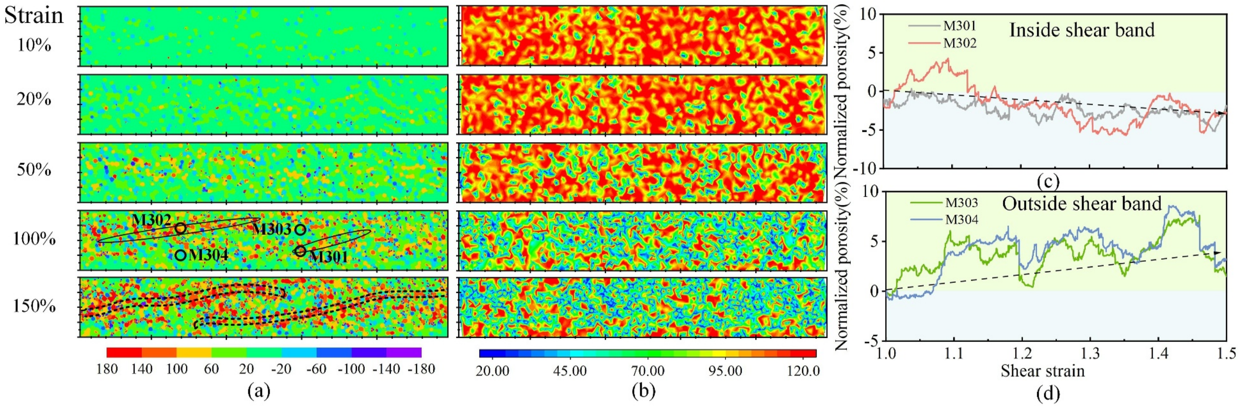

**Figure 9.** Maps of: (a) Cumulative grain rotation (Unit: °) with shear strain. (b) Grain size (Unit: μm). (c) and (d) Evolution of normalized porosity inside and outside the shear band at shear strains of 1.0–1.5 at $\sigma_n = 30$ MPa.

An increase in normal stress increases grain breakage with slip and rolling accommodating the shear deformation process. Significant compaction results, with notable correlation with grain size reduction (Figure 9). At low shear strains (<20%), the overall percentage of grain rotation remains low. As shear strain increases, numerous thin shear structures appear, migrate, then disappear, indicating the rapid evolution of shear structures as the macro shear bands begin to form (Figure 9a). At 150% strain, two low-angle shear bands form in the sample (marked by black dotted lines in Figure 8a), accompanied by a more localized porosity distribution. Obvious grain breakage appears within the shear band, indicating compaction localization. Due to the relatively lower intensity of grain breakage outside the shear band, a slight dilation occurs after 100% shear strain (Figures 9c and 9d), which is also observed in experimental results (Alikarami et al., 2015; Shahin & Hurley, 2022). Combined with the porosity distribution, an increase in shear strain results in a decrease in the average porosity and also a lower discrete deviation in the entire distribution of porosity (Figure 8b).

A continued increase in normal stress to $\sigma_n = 40$ MPa leads to a more significant shear compaction by grain breakage and both porosity and grain size show more obvious correlations (Figure 10). Compared with $\sigma_n = 30$ MPa at a shear strain of 100%, the zone of concentrated grain rotation is more localized. A large number of thin shear structures appear, accompanied by a significant reduction in grain size (Figure 10a). By terminal strain (for this experiment), multiple low-angle shear bands have developed. The increased normal stress results in more severe grain breakage, further intensifying the compaction inside the shear band and with dilation outside the shear band weakened (Figure 10d). With increasing shear strain, the average porosity decreases significantly, and the dispersion in overall porosity shows a clear trend of decreasing (Figure 8c).

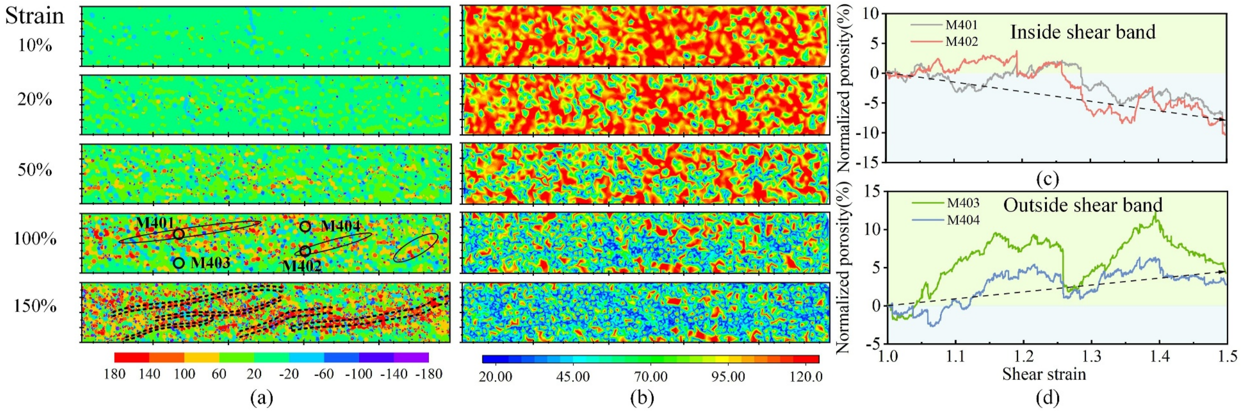

**Figure 10.** Maps of: (a) Cumulative grain rotation (Unit: °) with shear strain. (b) Grain size (Unit: μm) (c)–(d) Evolution of normalized porosity inside and outside the shear band at shear strains of 1.0–1.5 at $\sigma_n = 40$ MPa.

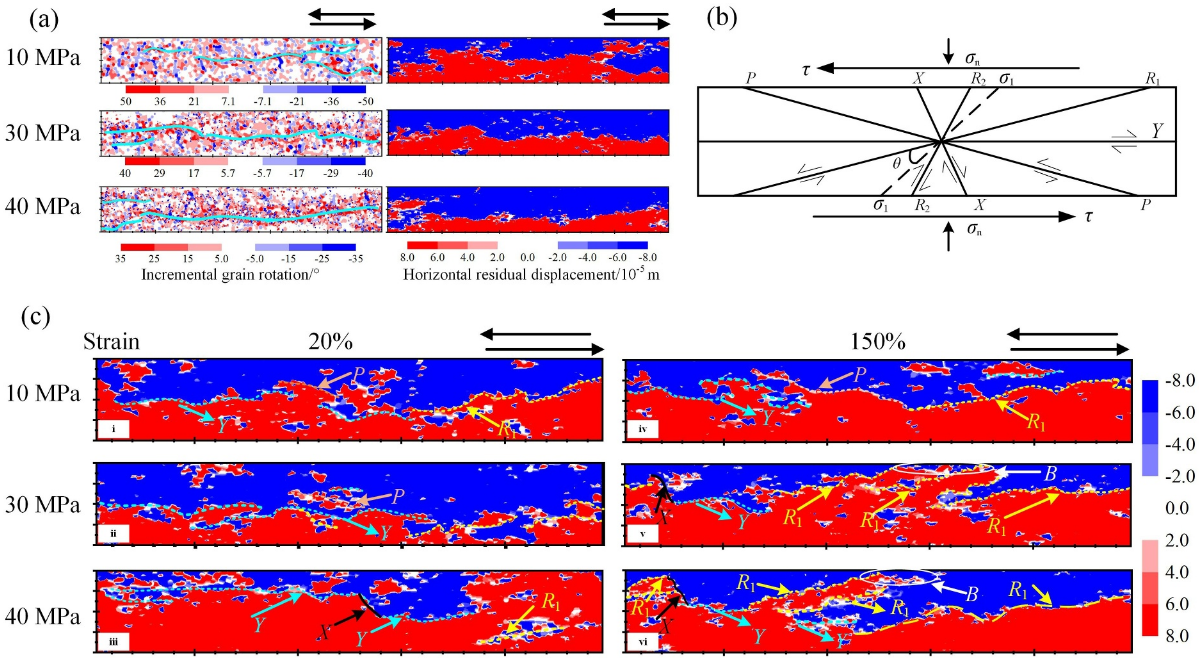

**Figure 11.** Evolving microstructures in shear bands: (a) Comparison of incremental grain rotation and residual shear displacement at 50% shear strain under different normal stresses. (b) Schematic describing shear microstructure. (c) Shear Microstructures revealed by horizontal residual displacements (Unit: $10^{-5}$ m).

### 3.4. Shear Band Microstructures

The residual displacement is the difference between the actual displacement of the grain and the displacement due to homogeneous shear strain over a given strain increment by Morgan and Boettcher (1999a) (Figure S1 in Supporting Information S1). To more clearly highlight the structural discontinuities, we select the horizontal component of the residual displacement for analysis. Consequently, the geometrical pattern of major shear structure and its evolution could be captured by examining the contours of horizontal residual displacement. The red and blue distributions (Figure 11) represent positive (follows the shear direction) and negative (opposite to the shear direction) residual displacements, respectively. Darker colors indicate larger residual shear displacement magnitudes, indicating continuous deformation. White marks the transition region between the positive and negative horizontal residual displacement regions, representing heterogeneous deformation. To verify the accuracy of this method, we also plot the distribution of incremental rotation and horizontal residual displacement at 10% strain increment in Figure 11a. The incremental grain rotation field is near identical to the residual shear displacement field, identifying that it is feasible to localize the shear microstructures from the pattern of horizontal residual displacements.

Furthermore, these microstructures can be classified based on their orientation and pattern as shown in Figure 11b (Logan et al., 1992; Volpe et al., 2022). Sub-horizontal *Y* shears are widespread throughout the simulation as one of the main distributed shear structures. At $\sigma_n = 10$ MPa, *Y* shears are concentrated in the center of the sample, forming multiple major *Y* shears. Broken grains at high normal stress provide more slip pathways, with *Y* shears relatively dispersed and with significant shear boundaries (Figure 11c(i)). After the termination of shearing, the low-angle *P* shears and low-angle $R_1$ shears nucleate into *Y* shears under low normal stress, and the large *Y* shears gradually split into discontinuous slip surfaces by other shear events, with significant boundary shear under high normal stress (Figures 11c(v) and 11c(vi)).

Low-angle $R_1$ shears are also active throughout the entire slip and are especially well developed at high normal stress (Figures 11c(v) and 11c(vi)). Some of the newly generated $R_1$ shears connect with the boundary shears, while others develop by the transfer and extension of the original $R_1$ shears. The number of $R_1$ shears increases gradually with the increase of normal stress. All of these $R_1$ shears show clear preferred orientations, having a low angle with the direction of shear (*X*-direction). At $\sigma_n = 10$ MPa, the $R_1$ shears are inclined at ~8°. With increased normal stress, the angle gradually increases and the $R_1$ shears rotate to ~9–11° at $\sigma_n = 30$ MPa and to ~12–16° at

$\sigma_n = 40$ MPa. The existence of periodic boundaries in our simulations (in the *X*-direction) often results in some low angle $R_1$ shears. Easier-to-distinguish $R_1$ shears develop at higher angles within the shear bands, especially at high normal stress, and are closer to the ~15–20° $R_1$ shears observed in many natural shear structures (Logan et al., 1992).

*P* shears are mainly active at $\sigma_n = 10$ MPa and low shear strains (Figures 11c(i) and 11c(ii)). As shear strain increases, some of the *P* shears connect with other shear structures and extend to form *Y* or $R_1$ shears (Figure 11c (iv)), while others gradually disappear (Figure 11c (v)). In addition, we occasionally observe that there are *X* shears, especially at high normal stress and high shear strains, with angles reaching 100–110°. However, they are often connected to other shear structures such as *Y* shears $R_1$ shears (Figures 11c(iii)–11c(vi)).

In order to verify that the orientation of the shear structure in our simulations is consistent with properties of the given material, we calculate the geometrical parameters of the shear microstructure for the given material. The inclination of shear structure ($\theta$) with respect to the maximum compressive principal stress (compression taken positive) varies between limits $\theta_c \le \theta \le \theta_R$, where $\theta_R$ and $\theta_c$ are given by the Roscoe and Coulomb formulae as (Han & Drescher, 1993)

$$\theta_c = \frac{\pi}{4} - \frac{\varphi_f}{2} \quad \theta_R = \frac{\pi}{4} - \frac{\psi}{2} \tag{7}$$

where $\varphi_f = \arctan \mu_f$, $\psi$ is the dilatancy angle. The friction strength of the gouge, $\mu_f$, will affect the orientation of the shear structure. As can be seen in Figure 2c, $\mu_f$ increases from low to high normal stresses in the simulation. According to the results of similar experiments under similar conditions (Gu & Wong, 1994; Morgan & Boettcher, 1999a), principal stress orientations vary between 45° and 50°. The maximum dilatancy angle varies between ~5°($\sigma_n = 10$ MPa) to 0° ($\sigma_n = 30$ and 40 MPa). By using Equation 7, the values of $\theta_c$, can be evaluated as 35–38° from high to low normal stress, and the theoretical $R_1$ shears are oriented 7–12° ($\sigma_n = 10$ MPa), 9–15° ($\sigma_n = 30$ MPa), and 10–16° ($\sigma_n = 40$ MPa). *P* shears develop in conjugate orientations symmetric to the $R_1$ shears. These orientations are consistent with those observed in our simulations.

## 4. Discussion

### 4.1. Grain Breakage Mechanisms

Normal stress impacts grain breakage in fault gouges (Abe & Mair, 2009; Guo & Morgan, 2006; Marone & Scholz, 1989). Breakage of quartz grains is greater during shear deformation, exhibiting grain exfoliation at a normal stress of 25 MPa and grain fragmentation at a normal stress of 100 MPa (Marone & Scholz, 1989). Three-dimensional DEM models of shear slip indicate that grain splitting dominates at high normal stress and low shear strain, while grain abrasion dominates at low normal stress and high shear strain (Mair & Abe, 2008). Consistent with these findings, our results also demonstrate a dependence of the degree of grain breakage on normal stress. At high normal stress, the degree of grain breakage is higher and with a correspondingly greater reduction in average grain size—further increasing the grain contact area. In addition, the evolution of the average grain size shows two stages at high normal stress: a fast decrease in the average grain size in the first stage, followed by a slow decrease, especially at $\sigma_n = 50$ MPa (Figure 4b). This represents a gradual transition of the grain size reduction mechanism from a predominantly high efficiency splitting to low efficiency abrasion (Figure 12). In contrast, at low normal stresses, the average grain size decreases slowly, indicating that the grain breakage mechanism is dominated by grain abrasion. Thus, the two grain breakage mechanisms lead to different evolutionary trends of grain size under different normal stress (Mair & Abe, 2011).

Also noted is that the transition between the two mechanisms begins earlier as the normal stress increases (Figure 12) and that the fractal dimension growth rate gradually slows down with increasing shear strain (Figures 5b–5d). No such transition is observed at low normal stress (Figure 5b) where the fractal dimension grows linearly (Figure 5a), due to the continuous abrasion of the grains. In the early stages of shear slip, the fault gouge under higher normal stress experiences more intense grain breakage. Conversely, the internal heterogeneity of the grains results in higher strength recovery of the broken grains which are increasingly more difficult to break. Meanwhile, the single particles formed by breakage cannot be further broken. Regarding the stress state, when smaller grains provide infill within the fault gouge, the large grains gain more contacts, resulting in a transition from point contact to uniform stresses between grains. This redistribution stabilizes their stress state and

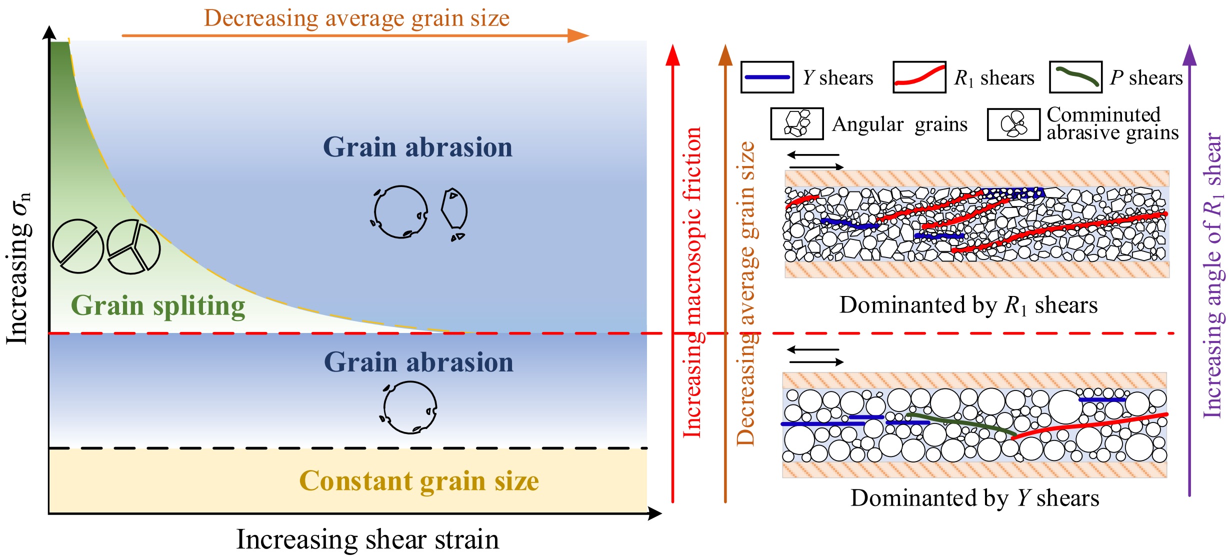

**Figure 12.** Schematic of grain breakage mechanisms and microstructural evolution.

reduces the potential for further breakage of the grains (Pizzati et al., 2020). Therefore, the increase of smaller grains with higher strength and the change in the stress state due to the increase of contact areas combine to promote an earlier transition from grain splitting to abrasion.

Although we explore the influence of normal stress and shear strain on the evolution of grain breakage mechanisms (abrasion and splitting) from grain size evolution, full investigation of the microscale evolution between local (particle-particle) failure and the grain breakage mechanisms in the shear band requires use of a higher resolution (comminution) model and is beyond the scope of this work.

### 4.2. Shear Deformation and Grain Breakage

Laboratory observations suggest that grain breakage plays an important role in the evolution of deformation during shear (Hunfeld et al., 2017; Mair et al., 2002). The decrease in average grain size and heterogeneous distribution of grain size caused by grain breakage ultimately promotes localized deformation. In our simulations, the degree of grain breakage increases overall with an increase in normal stress. Significant heterogeneity develops with an increase in shear strain. At low normal stress, the grains remain unbroken or are dominated by grain abrasion and the shear deformation is mainly accommodated by grain slip and rolling, concentrated within the central part of the sample (Figure 7a). At high normal stress, numerous angular grains develop due to grain splitting in the initial shear stage, restraining both grain slip and rolling. This leads to changes in the distribution of the contact forces and the redistribution of the contact stress. As shear strain increases, the angular grains formed by breakage become rounded and form fine grain layers as a result of continued abrasion (Figure 12). This enhances the rotation of the grains, allowing them to develop localized zones with high rotational concentrations that accommodate greater shear strain and ultimately develop shear bands with a dominant orientation. Morgan and Boettcher (1999b) assumed that rough angular grains restrain rolling and increase frictional resistance with neighboring grains, leading to angular grains clogging and locking the structure. And as intergranular resistance increases, grain slip decreases and grain rotation gradually enhances, while smaller particles are able to accommodate greater rotation after breakage. SEM observations after shear slip demonstrate that at $\sigma_n = 25$ MPa, breakage in glass beads is rare, with non-destructive processes (rolling and slip between grains) accommodating the majority of the shear strain. Glass beads undergo severe breakage at $\sigma_n = 40$ MPa, developing shear bands with specific orientations and decreased grain size (Mair et al., 2002). Additionally, our simulation results are consistent with field observations that shear bands tend to evolve a wider grain size gradation as a result of grain breakage (Pizzati et al., 2020).

### 4.3. Microstructural Characterization and Grain Breakage

An increase in normal stress, which promotes the evolution of grain size gradation and thus influences the localization of shear strain, has been demonstrated in experiments (De Paola et al., 2015; Shigematsu et al., 2004). Shear bands display certain geometrical characteristics with an increase in localization. Sub-horizontal discontinuous *Y* shears and $R_1$ shears develop throughout the early loading stages of the simulations. The gouge shows continuous dilation and develops independent low-angle *P* shears at low normal stress (Figure 11c(i)). In contrast, the overall trend shifts toward compaction under high normal stress. Although *P* shears and high-angle *X* shears develop locally, they tend to connect with *Y* shears or $R_1$ shears, rather than forming independent structures (Figure 11c(ii)). Our findings are in general agreement with laboratory observations of compaction in fault gouges due to breakage (Kenigsberg et al., 2019). In the laboratory, low-angle $R_1$ shears and *Y* shears are more apparent, with $R_1$ shears tending to develop earlier and *Y* shears persisting (Scuderi et al., 2017). In granular kinematics, *P* shears and *X* shears are adaptable to dilatation, while $R_1$ shears respond in compaction and *Y* shears for infinite shear strains (Roy et al., 2021). *P* shears and *X* shears are not well captured in the laboratory due to the limited methods and number of observations in the early stages of shear (Morgan & Boettcher, 1999a). As the shear strain continues to increase, the *P* shears in the simulations are gradually captured by the $R_1$ shears and *Y* shears to form larger *Y* shears at low normal stress, accommodating much larger shear strains. With an increase in normal stress, we observe more $R_1$ shears at higher angles, conforming to the Coulomb failure criterion (Figure 12). These $R_1$ shears separate the *Y* shears and group arrays of $R_1$ shears (Figures 11c(v) and 11c(vi)), probably resulting from the redistribution of the stress field within the shear bands. This redistribution of the stress field is associated with the change in grain gradation, in turn resulting from the continuous grain breakage. In addition, localized boundary shears are observed in our simulations, especially at high normal stresses and high shear strains (Figures 11c(v) and 11c(vi)). These boundary shears tend to connect with $R_1$ shears, which is also similar to experimental observations (Hunfeld et al., 2020; Mair et al., 2002).

### 4.4. Limitations

Clearly, the current 2D model represents a simplification of the true 3D nature of deformation where particles are able to transit laterally out of the 2D plane of analysis. These deviations are small in comparison to the large deformations and shear strains that result in the 2D plane of analysis. Thus it is anticipated that similar modes of deformation occur in 2D as in 3D as constrained by the geometrically enforced 2D plane strain/deformation conditions - thus breakage and the evolution of texture in 2D should largely align with that anticipated in the 3D system. Minor differences may result. However, this study does not consider the effects of size segregation during grain size evolution, and the intergranular fluid is also excluded, both of which could potentially impact the shear behavior within the grains (Cui et al., 2021). Future work will focus on developing a 3D DEM that couples fluid effects, predicting the patterns of grain segregation within shear bands. Furthermore, our simulations also focus on the influence of normal stress on fault fracture and deformation, further illuminating physical experiments. However, since the stiffness of the surrounding rock in the geological environment is ignored, it may lead to certain differences from the actual geological sites.

## 5. Conclusions

We utilize a granular mechanics model (DEM) that accommodates grain breakage in shear-deformed gouges to explore the impacts of confining stress on compaction and dilation modes and the evolution of microstructures. We also link the mechanics of fault friction properties to the evolution of porosity. We follow the evolution of microstructural evolution and the appearance of shear bands. In particular, we link elevated normal stresses to the suppression of dilation and a switch from dilation based structural reorganization of the particulate assemble to compaction-based suppression that is aided by grain breakage. The major findings of this work can be summarized as follows:

An increase of normal stress promotes grain breakage and reduces grain size while simultaneously increasing the angularity of grains that limits contact sliding, leading to an increase in macroscopic frictional strength. The rearrangement of grains destroys strong force chains, promoting large slip events at low normal stress. Grain breakage induces localized failure of force chains, resulting in numerous small slip events. This ultimately enhances the overall stability of the force chain network, thereby reducing the occurrence of large slip events.

Grain breakage restrains volume dilation that is promoted by structural rearrangement and transforms response into a compaction dominated mode with a monotonic decrease in average porosity. Simultaneously, the heterogeneous comminution of grains affects the porosity distribution, leading to a transition from dilation to compaction within the shear band, in turn resulting in the localization of strain within shear zones.

An increase in normal stress results in the evolution of grain size distribution from a uniform to a fractal distribution, approaching a terminal fractal dimension of 2.55 in our simulations. At low normal stress, grain breakage is dominated by abrasion from the grain surface, and the average grain size decreases slowly. At high normal stress, the principal mechanism gradually transitions from abrasion to splitting and the average grain size correspondingly decreases rapidly. An increase in shear strain, corresponding increase in the number of smaller grains with higher strength and change in the stress state due to the increase in net contact area combine to promote an earlier transition from grain splitting to abrasion.

Grain breakage is a key control of shear deformation in the gouge. At low normal stress, the grain deformation is mainly accommodated by slipping and rolling and evolves along central axis of the sample. At high normal stress, grain breakage is the primary response during shear deformation. The development of shear bands is accompanied by a reduction in grain size and porosity. As shear strain increases, the angular grains formed by breakage are rounded and form fine grained layers as a result of continued abrasion. Thus, grain rotations in this fine-grained zone are significantly enhanced to accommodate much larger shear deformation.

Grain breakage also profoundly affects the evolution of microstructures in the evolution of shear bands. $Y$ shears and low angle $R_1$ shears are widespread throughout the simulations. Low angle $P$ shears and high angle $X$ shears, which likely accommodate local shear band dilation are captured by the $R_1$ shears and $Y$ shears at terminal strain. At low normal stress, the shear bands are dominated by $Y$ shears. With an increase in normal stress, grain breakage results in the redistribution of the stress field in and around the shear bands, promoting the development of the more highly inclined $R$ shears.

## Data Availability Statement

We use the DEM Particle Flow Code 2D software (PFC2D, version 6.0) from Itasca Consulting Group, Ltd. to implement our model application (https://www.itascacg.com/software/PFC). The numerical codes and the numerical data obtained in this study are available at Zenodo via (Li Q, 2024) with open access.

**Acknowledgments**
This study was supported by the China National Key Research and Development Program (Grant: 2021YFC3000603), the Natural Science Foundation of China (Grant 5217041034, 42477213), $CO_2$ Enhanced Shale Gas Recovery and Sequestration by Numerical Thermal-Hydro-Mechanical-Chemical Modelling (Grant: 2023DQ02-0206) and Deep Earth Probe and Mineral Resources Exploration-National Science and Technology Major Project (2024ZD1000704), the Fundamental Research Funds for the Central Universities (Grant 2023CDJKYJH041).

## References

Abe, S., & Mair, K. (2005). Grain fracture in 3D numerical simulations of granular shear. *Geophysical Research Letters*, *32*(5), L5305. https://doi.org/10.1029/2004GL022123

Abe, S., & Mair, K. (2009). Effects of gouge fragment shape on fault friction: New 3D modelling results. *Geophysical Research Letters*, *36*(23), 1–4. https://doi.org/10.1029/2009GL040684

Aharonov, E., & Sparks, D. (2004). Stick-slip motion in simulated granular layers. *Journal of Geophysical Research*, *109*(B9), B9306. https://doi.org/10.1029/2003JB002597

Alikarami, R., Ando, E., Gkiousas-Kapnisis, M., Torabi, A., & Viggiani, G. (2015). Strain localisation and grain breakage in sand under shearing at high mean stress; insights from in situ X-ray tomography. *Acta Geotechnica*, *10*(1), 15–30. https://doi.org/10.1007/s11440-014-0364-6

Anthony, J. L., & Marone, C. (2005). Influence of particle characteristics on granular friction. *Journal of Geophysical Research*, *110*(B8), 1–14. https://doi.org/10.1029/2004JB003399

Balsamo, F., & Storti, F. (2010). Grain size and permeability evolution of soft-sediment extensional sub-seismic and seismic fault zones in high-porosity sediments from the Crotone Basin, Southern Apennines, Italy. *Marine and Petroleum Geology*, *27*(4), 822–837. https://doi.org/10.1016/j.marpetgeo.2009.10.016

Billi, A., Salvini, F., & Storti, F. (2003). The damage zone-fault core transition in carbonate rocks: Implications for fault growth, structure and permeability. *Journal of Structural Geology*, *25*(11), 1779–1794. https://doi.org/10.1016/S0191-8141(03)00037-3

Bolton, M. D., Nakata, Y., & Cheng, Y. P. (2008). Micro- and macro-mechanical behaviour of DEM crushable materials. *Géotechnique*, *58*(6), 471–480. https://doi.org/10.1680/geot.2008.58.6.471

Boulton, C., Yao, L., Faulkner, D. R., Townend, J., Toy, V. G., Sutherland, R., et al. (2017). High-velocity frictional properties of Alpine Fault rocks: Mechanical data, microstructural analysis, and implications for rupture propagation. *Journal of Structural Geology*, *97*, 71–92. https://doi.org/10.1016/j.jsg.2017.02.003

Casas, N., Mollon, G., & Daouadji, A. (2023). Influence of grain-scale properties on localization patterns and slip weakening within dense granular fault gouges. *Journal of Geophysical Research: Solid Earth*, *128*(3), 1–23. https://doi.org/10.1029/2022JB025666

Cheng, Y. P., Nakata, Y., & Bolton, M. D. (2003). Discrete element simulation of crushable soil. *Géotechnique*, *53*(7), 633–641. https://doi.org/10.1680/geot.2003.53.7.633

Chin, L. Y., Raghavan, R., & Thomas, L. K. (2000). Fully coupled geomechanics and fluid-flow analysis of wells with stress-dependent permeability. *SPE Journal*, *5*(1), 32–45. https://doi.org/10.2118/58968-PA

Cui, K. F. E., Zhou, G. G. D., & Jing, L. (2021). Viscous effects on the particle size segregation in geophysical mass flows: Insights from immersed granular shear flow simulations. *Journal of Geophysical Research: Solid Earth*, *126*(8), 1–21. https://doi.org/10.1029/2021JB022274

Del Sole, L., & Antonellini, M. (2019). Microstructural, petrophysical, and mechanical properties of compactive shear bands associated to calcite cement concretions in arkose sandstone. *Journal of Structural Geology*, *126*, 51–68. https://doi.org/10.1016/j.jsg.2019.05.007

De Paola, N., Holdsworth, R. E., Viti, C., Collettini, C., & Bullock, R. (2015). Can grain size sensitive flow lubricate faults during the initial stages of earthquake propagation? *Earth and Planetary Science Letters*, *431*, 48–58. https://doi.org/10.1016/j.epsl.2015.09.002

Dor, O., Ben-Zion, Y., Rockwell, T. K., & Brune, J. (2006). Pulverized rocks in the Mojave section of the San Andreas fault zone. *Earth and Planetary Science Letters*, *245*(3), 642–654. https://doi.org/10.1016/j.epsl.2006.03.034

Dorostkar, O., & Carmeliet, J. (2019). Grain friction controls characteristics of seismic cycle in faults with granular gouge. *Journal of Geophysical Research: Solid Earth*, *124*(7), 6475–6489. https://doi.org/10.1029/2019JB017374

Ferdowsi, B., Griffa, M., Guyer, R. A., Johnson, P. A., Marone, C., & Carmeliet, J. (2014). 3D Discrete Element Modeling of triggered slip in sheared granular media. *Physical Review*, *89*(4), 1–12. https://doi.org/10.1103/PhysRevE.89.042204

Frye, K. M., & Marone, C. (2002). The effect of particle dimensionality on granular friction in laboratory shear zones. *Geophysical Research Letters*, *29*(19), 1–4. https://doi.org/10.1029/2002GL015709

Fukuoka, H. (1991). Variation of the friction angle of granular materials in the high-speed high-stress ring-shear apparatus, Influence of re-orientation, alignment and crushing of grains during shear. *Annuals of the Disaster Prevention Research Institute*, *41*(4), 243–279. https://doi.org/10.11501/3088538

Fukuoka, H., Sassa, K., & Wang, G. (2007). Influence of shear speed and normal stress on the shear behavior and shear zone structure of granular materials in naturally drained ring shear tests. *Landslides*, *4*(1), 63–74. https://doi.org/10.1007/s10346-006-0053-0

Goldenberg, C., & Goldhirsch, I. (2005). Friction enhances elasticity in granular solids. *Nature*, *435*(7039), 188–191. https://doi.org/10.1038/nature03497

Gu, X. Q., Huang, M. S., & Qian, J. G. (2014). Discrete element modeling of shear band in granular materials. *Theoretical and Applied Fracture Mechanics*, *72*, 37–49. https://doi.org/10.1016/j.tafmec.2014.06.008

Gu, Y. J., & Wong, T. F. (1994). Development of shear localization in simulated quartz gouge: Effects of cumulative slip and gouge particle size. *Pure and Applied Geophysics*, *143*(1/2/3), 387–423. https://doi.org/10.1007/BF00874336

Guo, Y. G., & Morgan, J. K. (2006). The frictional and micromechanical effects of grain comminution in fault gouge from distinct element simulations. *Journal of Geophysical Research*, *111*(B12406). https://doi.org/10.1029/2005JB004049

Han, C. H., & Drescher, A. (1993). Shear bands in biaxial tests on dry coarse sand. *Soils and Foundations*, *33*(1), 118–132. https://doi.org/10.3208/sandf1972.33.118

Han, R., Hirose, T., & Shimamoto, T. (2010). Strong velocity weakening and powder lubrication of simulated carbonate faults at seismic slip rates. *Journal of Geophysical Research*, *115*(B3), B3412. https://doi.org/10.1029/2008JB006136

Hunfeld, L. B., Chen, J. Y., Hol, S., Niemeijer, A. R., & Spiers, C. J. (2020). Healing behavior of simulated fault gouges from the Groningen Gas Field and implications for induced fault reactivation. *Journal of Geophysical Research: Solid Earth*, *125*(7), e2019JB018790. https://doi.org/10.1029/2019JB018790

Hunfeld, L. B., Niemeijer, A. R., & Spiers, C. J. (2017). Frictional properties of simulated fault gouges from the seismogenic Groningen Gas Field under in situ P–T -Chemical conditions. *Journal of Geophysical Research: Solid Earth*, *122*(11), 8969–8989. https://doi.org/10.1002/2017JB014876

Itasca Consulting Group Inc. (2019). Particle flow code. *version* 6.0.

Kenigsberg, A. R., Rivière, J., Marone, C., & Saffer, D. M. (2019). The effects of shear strain, fabric, and porosity evolution on elastic and mechanical properties of clay-rich Fault Gouge. *Journal of Geophysical Research: Solid Earth*, *124*(11), 968–982. https://doi.org/10.1029/2019JB017944

Koval, G., Roux, J. N., Corfdir, A., & Chevoir, F. (2009). Annular shear of cohesionless granular materials: From the inertial to quasistatic regime. *Physical Review*, *79*(2), 21306. https://doi.org/10.1103/PhysRevE.79.021306

Kuo, L. W., Li, H., Smith, S. A., Di Toro, G., J. Suppe, S. R. S., Song, S. R., et al. (2014). Gouge graphitization and dynamic fault weakening during the 2008 Mw 7.9 Wenchuan earthquake. *Geology*, *42*(1), 47–50. https://doi.org/10.1130/G34862.1

Li, Q. (2024). Controls of grain breakage on shear band morphology and porosity evolution in fault gouges. *Zenodo*. [Dataset]. https://doi.org/10.5281/zenodo.15114071

Li, Y., Hu, W., Xu, Q., Huang, R., Chang, C., Chen, J., & Wang, Y. (2024). Velocity profile geometries and granular temperature distributions in very dense granular flows. *Geophysical Research Letters*, *51*(2), 1–10. https://doi.org/10.1029/2023GL104410

Lin, J., Bauer, E., & Wu, W. (2020). A combined method to model grain crushing with DEM. *Geoscience Frontiers*, *11*(2), 451–459. https://doi.org/10.1016/j.gsf.2019.02.011

Liu, J. Y., Nicot, F., & Zhou, W. (2018). Sustainability of internal structures during shear band forming in 2D granular materials. *Powder Technology*, *338*, 458–470. https://doi.org/10.1016/j.powtec.2018.07.001

Liu, Y., Wang, X., & Yu, P. (2020). Critical state of granular materials at mesoscale; transition from local to global. *International Journal for Numerical and Analytical Methods in Geomechanics*, *44*(12), 1676–1694. https://doi.org/10.1002/nag.3084

Logan, J. M., Dengo, C. A., Higgs, N. G., & Wang, Z. Z. (1992). Fabrics of experimental fault zones; their development and relationship to mechanical behavior. *International Geophysics*, *51*, 33–67. https://doi.org/10.1016/s0074-6142(08)62814-4

Long, J. T., Morgan, J. K., & Dugan, B. (2018). Microstructural evolution of porosity and stress during the formation of brittle shear fractures: A discrete element model study. *Journal of Geophysical Research: Solid Earth*, *123*(3), 2228–2245. https://doi.org/10.1002/2017JB014842

Lyu, Z., Rivière, J., Yang, Q., & Marone, C. (2019). On the mechanics of granular shear: The effect of normal stress and layer thickness on stick-slip properties. *Tectonophysics*, *763*, 86–99. https://doi.org/10.1016/j.tecto.2019.04.010

Mair, K., & Abe, S. (2008). 3D numerical simulations of fault gouge evolution during shear: Grain size reduction and strain localization. *Earth and Planetary Science Letters*, *274*(1–2), 72–81. https://doi.org/10.1016/j.epsl.2008.07.010

Mair, K., & Abe, S. (2011). Breaking up: Comminution mechanisms in sheared simulated fault gouge. *Pure and Applied Geophysics*, *168*(12), 2277–2288. https://doi.org/10.1007/s00024-011-0266-6

Mair, K., Frye, K. M., & Marone, C. (2002). Influence of grain characteristics on the friction of granular shear zones. *Journal of Geophysical Research*, *107*(B10), ECV41–ECV49. https://doi.org/10.1029/2001jb000516

Marone, C., & Scholz, C. H. (1989). Particle-size distribution and microstructures within simulated fault gouge. *Journal of Structural Geology*, *11*(7), 799–814. https://doi.org/10.1016/0191-8141(89)90099-0

MiDi, G. (2004). On dense granular flows. *The European Physical Journal E*, *14*(4), 341–365. https://doi.org/10.1140/epje/i2003-10153-0

Mollon, G., Quacquarelli, A., Andò, E., & Viggiani, G. (2020). Can friction replace roughness in the numerical simulation of granular materials? *Granular Matter*, *22*(2), 1–16. https://doi.org/10.1007/s10035-020-1004-5

Mora, P., & Place, D. (1998). Numerical simulation of earthquake faults with gouge; toward a comprehensive explanation for the heat flow paradox. *Journal of Geophysical Research*, *103*(B9), 21067–21089. https://doi.org/10.1029/98JB01490

Morgan, J. K., & Boettcher, M. S. (1999a). Numerical simulations of granular shear zones using the distinct element method; 1, Shear zone kinematics and the micromechanics of localization. *Journal of Geophysical Research*, *104*(B2), 2703–2719. https://doi.org/10.1029/1998JB900056

Morgan, J. K., & Boettcher, M. S. (1999b). Numerical simulations of granular shear zones using the distinct element method 2. Effects of particle size distribution and interparticle friction on mechanical behavior. *Journal of Geophysical Research*, *104*(B2), 2721–2732. https://doi.org/10.1029/1998JB900056

Muto, J., Nakatani, T., Nishikawa, O., & Nagahama, H. (2015). Fractal particle size distribution of pulverized fault rocks as a function of distance from the fault core. *Geophysical Research Letters*, *42*(10), 3811–3819. https://doi.org/10.1002/2015GL064026

Nakata, Y., Kato, Y., Hyodo, M., Hyde, A. F. L., & Murata, H. (2001). One-Dimensional compression behaviour of uniformly Graded Sand related to single particle crushing strength. *Soils and Foundations*, *41*(2), 39–51. https://doi.org/10.3208/sandf.41.2_39

Nie, Z. H., Huang, C. H., Zhao, P. P., & Fang, C. F. (2023). Influence of the interparticle friction coefficient on the mechanical behaviour of breakable granular materials with realistic shape. *Advanced Powder Technology*, *34*(11), 104223. https://doi.org/10.1016/j.apt.2023.104223

O'Sullivan, C., & Bray, J. D. (2004). Selecting a suitable time step for discrete element simulations that use the central difference time integration scheme. *Engineering Computations*, *21*(2/3/4), 278–303. https://doi.org/10.1108/02644400410519794

Papachristos, E., Stefanou, I., & Sulem, J. (2023). A discrete elements study of the frictional behavior of fault gouges. *Journal of Geophysical Research: Solid Earth*, *128*(1), 1–25. https://doi.org/10.1029/2022JB025209

Pizzati, M., Balsamo, F., & Storti, F. (2020). Displacement-dependent microstructural and petrophysical properties of deformation bands and gouges in poorly lithified sandstone deformed at shallow burial depth (Crotone Basin, Italy). *Journal of Structural Geology*, *137*, 104069. https://doi.org/10.1016/j.jsg.2020.104069

Potyondy, D. O., & Cundall, P. A. (2004). A bonded-particle model for rock. *International Journal of Rock Mechanics and Mining Sciences*, *41*(8), 1329–1364. https://doi.org/10.1016/j.ijrmms.2004.09.011

Ran, X. Y., Xu, F. Y., & Wang, A. X. (2022). One-dimensional compression characteristics of uniformly graded sand under high stresse. *Granular Matter*, *24*(2), 5–12. https://doi.org/10.1007/s10035-022-01213-x

Rinaldi, A. P., Rutqvist, J., & Cappa, F. (2014). Geomechanical effects on $CO_2$ leakage through fault zones during large-scale underground injection. *International Journal of Greenhouse Gas Control*, *20*, 117–131. https://doi.org/10.1016/j.ijggc.2013.11.001

Roy, A., Roy, N., Saha, P., & Mandal, N. (2021). Factors determining shear-parallel versus low-angle shear band localization in shear deformations: Laboratory experiments and numerical simulations. *Journal of Geophysical Research: Solid Earth*, *126*(10), 1–23. https://doi.org/10.1029/2021JB022578

Schultz, R. A., Okubo, C. H., & Fossen, H. (2010). Porosity and grain size controls on compaction band formation in Jurassic Navajo Sandstone. *Geophysical Research Letters*, *37*(22), 1–5. https://doi.org/10.1029/2010GL044909

Scuderi, M. M., Collettini, C., Viti, C., Tinti, E., & Marone, C. (2017). Evolution of shear fabric in granular fault gouge from stable sliding to stick slip and implications for fault slip mode. *Geology*, *45*(8), 731–734. https://doi.org/10.1130/G39033.1

Shahin, G., & Hurley, R. C. (2022). Micromechanics and strain localization in sand in the ductile regime. *Journal of Geophysical Research: Solid Earth*, *127*(11), 1–19. https://doi.org/10.1029/2022JB024983

Shigematsu, N., Fujimoto, K., Ohtani, T., & Goto, K. (2004). Ductile fracture of fine-grained plagioclase in the brittle–plastic transition regime: Implication for earthquake source nucleation. *Earth and Planetary Science Letters*, *222*(3), 1007–1022. https://doi.org/10.1016/j.epsl.2004.04.001

Smith, S. A., Billi, A., Toro, G. D., & Spiess, R. (2011). Principal slip zones in limestone: Microstructural characterization and implications for the seismic cycle (Tre Monti fault, central Apennines, Italy). *Pure and Applied Geophysics*, *168*(12), 2365–2393. https://doi.org/10.1007/s00024-011-0267-5

Storti, F., Billi, A., & Salvini, F. (2003). Particle size distributions in natural carbonate fault rocks: Insights for non-self-similar cataclasis. *Earth and Planetary Science Letters*, *206*(1–2), 173–186. https://doi.org/10.1016/S0012-821X(02)01077-4

Thornton, C. (2000). Numerical simulations of deviatoric shear deformation of granular media. *Géotechnique*, *50*(1), 43–53. https://doi.org/10.1680/geot.2000.50.1.43

Torabi, A., Braathen, A., Cuisiat, F., & Fossen, H. (2007). Shear zones in porous sand; insights from ring shear experiments and naturally deformed sandstones. *Tectonophysics*, *437*(1–4), 37–50. https://doi.org/10.1016/j.tecto.2007.02.018

Turcotte, D. L. (1983). Fractals and fragmentation. *Journal of Geophysical Research*, *91*(B2), 1921–1926. https://doi.org/10.1029/JB091iB02p01921

van den Ende, M. P. A., & Niemeijer, A. R. (2018). Time-dependent compaction as a mechanism for regular stick-slips. *Geophysical Research Letters*, *45*(12), 5959–5967. https://doi.org/10.1029/2018GL078103

Volpe, G., Pozzi, G., & Collettini, C. (2022). Y-B-P-R or S-C-C′? Suggestion for the nomenclature of experimental brittle fault fabric in phyllosilicate-granular mixtures. *Journal of Structural Geology*, *165*, 104743. https://doi.org/10.1016/j.jsg.2022.104743

Wang, C. Y., Elsworth, D., & Fang, Y. (2019). Ensemble shear strength, stability, and permeability of mixed mineralogy fault gouge recovered from 3D granular models. *Journal of Geophysical Research: Solid Earth*, *124*(1), 425–441. https://doi.org/10.1029/2018JB016066

Wang, D., Carmeliet, J., Zhou, W., & Dorostkar, O. (2021). On the effect of grain fragmentation on frictional instabilities in faults with granular gouge. *Journal of Geophysical Research: Solid Earth*, *126*(5), 1–20. https://doi.org/10.1029/2020JB020510

Wang, J. F., & Yan, H. B. (2012). DEM analysis of energy dissipation in crushable soils. *Soils and Foundations*, *52*(4), 644–657. https://doi.org/10.1016/j.sandf.2012.07.006

Wang, J. F., & Yan, H. B. (2013). On the role of particle breakage in the shear failure behavior of granular soils by DEM. *International Journal for Numerical and Analytical Methods in Geomechanics*, *37*(8), 832–854. https://doi.org/10.1002/nag.1124

Wong, T., & Baud, P. (2012). The brittle-ductile transition in porous rock: A review. *Journal of Structural Geology*, *44*, 25–53. https://doi.org/10.1016/j.jsg.2012.07.010

Zhang, F. S., An, M. K., Zhang, L. Y., Fang, Y., & Elsworth, D. (2020). Effect of mineralogy on friction-dilation relationships for simulated faults: Implications for permeability evolution in caprock faults. *Geoscience Frontiers*, *11*(2), 439–450. https://doi.org/10.1016/j.gsf.2019.05.014

Zhang, H., Hu, X., Wang, L., Zhao, E., & Liu, C. (2023). Effect mechanism of block convexity on the shear behaviors of soil-rock mixtures by the developed 3D spherical harmonics-based modeling approach. *Computers and Geotechnics*, *155*, 105183. https://doi.org/10.1016/j.compgeo.2022.105183

Zhang, T., Yu, L. T., Peng, Y. X., Ju, M. H., Yin, Q., Wei, J. B., & Jia, S. P. (2022). Influence of grain size and basic element size on rock mechanical characteristics: Insights from grain-based numerical analysis. *Bulletin of Engineering Geology and the Environment*, *81*(9), 1–23. https://doi.org/10.1007/s10064-022-02856-z

Zhou, W., Yang, L. F., Ma, G., Xu, K., Lai, Z. Q., & Chang, X. L. (2017). DEM modeling of shear bands in crushable and irregularly shaped granular materials. *Granular Matter*, *19*(2), 1–12. https://doi.org/10.1007/s10035-017-0712-y

Zhu, H., Nicot, F., & Darve, F. (2016). Meso-structure organization in two-dimensional granular materials along biaxial loading path. *International Journal of Solids and Structures*, *96*, 25–37. https://doi.org/10.1016/j.ijsolstr.2016.06.025